Energy Engineering

Tech Science Press

Doi:10.32604/ee.2025.063178

ARTICLE

Optimization of Supply and Demand Balancing in Park-Level Energy Systems Considering Comprehensive Utilization of Hydrogen under P2G-CCS Coupling

Zhiyuan Zhang[1], **Yongjun Wu**[1], **Xiqin Li**[1], **Minghui Song**[1], **Guangwu Zhang**[2], **Ziren Wang**[3,*] and **Wei Li**[3]

[1]State Grid Beijing Electric Power Company, Beijing, 102300, China
[2]State Grid Beijing Mentougou Power Supply Company, Beijing, 102300, China
[3]School of Economics and Management, North China Electric Power University, Baoding, 071003, China

*Corresponding Author: Ziren Wang. Email: wzr@ncepu.edu.cn

Received: 07 January 2025; Accepted: 14 March 2025; Published: 25 April 2025

ABSTRACT: The park-level integrated energy system (PIES) is essential for achieving carbon neutrality by managing multi-energy supply and demand while enhancing renewable energy integration. However, current carbon trading mechanisms lack sufficient incentives for emission reductions, and traditional optimization algorithms often face challenges with convergence and local optima in complex PIES scheduling. To address these issues, this paper introduces a low-carbon dispatch strategy that combines a reward-penalty tiered carbon trading model with P2G-CCS integration, hydrogen utilization, and the Secretary Bird Optimization Algorithm (SBOA). Key innovations include: (1) A dynamic reward-penalty carbon trading mechanism with coefficients (μ = 0.2, λ = 0.15), which reduces carbon trading costs by 47.2% (from \$694.06 to \$366.32) compared to traditional tiered models, incentivizing voluntary emission reductions. (2) The integration of P2G-CCS coupling, which lowers natural gas consumption by 41.9% (from \$4117.20 to \$2389.23) and enhances CO_2 recycling efficiency, addressing the limitations of standalone P2G or CCS technologies. (3) The SBOA algorithm, which outperforms traditional methods (e.g., PSO, GWO) in convergence speed and global search capability, avoiding local optima and achieving 24.39% faster convergence on CEC2005 benchmark functions. (4) A four-energy PIES framework incorporating electricity, heat, gas, and hydrogen, where hydrogen fuel cells and CHP systems improve demand response flexibility, reducing gas-related emissions by 42.1% and generating \$13.14 in demand response revenue. Case studies across five scenarios demonstrate the strategy's effectiveness: total operational costs decrease by 14.7% (from \$7354.64 to \$6272.59), carbon emissions drop by 49.9% (from 5294.94 to 2653.39 kg), and renewable energy utilization increases by 24.39% (from 4.82% to 8.17%). These results affirm the model's ability to reconcile economic and environmental goals, providing a scalable approach for low-carbon transitions in industrial parks.

KEYWORDS: Park-level integrated energy system; P2G-CCS coupling; comprehensive utilization of hydrogen; reward-penalty tiered carbon trading mechanism; secretary bird optimization algorithm

1 Introduction

The Park-level Integrated Energy System (PIES) plays a crucial role in carbon emissions resulting from energy consumption. It has the potential to improve energy efficiency, enhance supply reliability, and facilitate the advancement of smart grid technologies. As the depletion of global fossil energy sources looms and greenhouse gas emissions escalate, China's ambitions for "carbon peak" and "carbon neutrality" have gained international focus. In light of the dual carbon policy and growing social and environmental accountability, it is essential to conduct comprehensive research on operational improvement strategies for PIES in China. Consequently, the pursuit of low-carbon economic operations within PIES has emerged as a significant area of inquiry. Additionally, PIES incorporates various energy sources, catering to a wide range of user demands. Its capacity to effectively integrate and manage these different energy sources is vital for ensuring stable energy supply and balancing generation with consumption. Thus, collaborative studies on the low-carbon, cost-effective, and stable functioning of PIES are critically important.

Pioneering research on electricity-carbon nexus integration emerges in Reference [1], which establishes a foundational scheduling framework incorporating carbon emission trading mechanisms into multi-energy systems. This work introduces an interval-based tiered carbon pricing model that synergizes emission trading costs with external energy expenditures, formulating a tri-vector (electricity-heat-gas) low-carbon economic optimization paradigm. Reference [2] advances this paradigm through stochastic multi-objective optimization addressing renewable generation and load uncertainties, demonstrating through comparative analysis that adaptive carbon market participation achieves 22%–28% greater emission reductions than conventional approaches when implementing regionally calibrated pricing-quota configurations. Technological innovation pathways are explored in subsequent studies: Reference [3] demonstrates demand-flexible scheduling integrating P2G conversion with carbon market interactions, revealing 15%–20% simultaneous reductions in energy intensity and emissions through techno-economic simulations. Reference [4] extends system boundaries through a hydrogen-enabled bi-level planning model addressing temporal investment sequencing and carbon market dynamics, thereby establishing hydrogen-energy nexus optimization as critical infrastructure for cross-vector energy transitions. Collaborative system architectures receive attention in Reference [5], which develops a privacy-preserving distributed scheduling framework using cooperative game-theoretic energy sharing mechanisms, resolving the trilemma of resource optimization (35%–40% efficiency gains), data confidentiality, and equitable benefit allocation (Nash equilibrium solutions). Reference [6] implements advanced uncertainty management through hybrid PV/T-hydrogen systems coupled with enhanced carbon trading strategies, employing modified K-means clustering for scenario reduction that achieves 92% probability coverage with 60% fewer scenarios. System integration reaches new complexity in Reference [7]'s tri-level optimization model coordinating green hydrogen stations, fuel cell fleets, and dual-network (power/gas) operations, validated through multi-criteria analysis showing 18% cost reduction and 99.2% reliability metrics. These cumulative advancements establish three critical research trajectories: 1) dynamic carbon market coupling mechanisms, 2) cross-vector hydrogen integration strategies, and 3) distributed optimization frameworks for multi-stakeholder systems—each addressing fundamental challenges in renewable penetration (targeting 75%–85%) and decarbonization pathways (45%–55% reduction targets). Reference [8] delineates an integrative framework for synchronizing renewable energy deployment with carbon emission management in PIES, enabling optimized resource utilization through stochastic modeling of photovoltaic and aeolian generation uncertainties. Subsequent work by Reference [9] formulates a tiered carbon trading-embedded scheduling paradigm that demonstrates operational efficacy in balancing economic performance with emission reduction targets, though its oversight of wind-solar complementarity warrants critical examination. The transactional dimension of PIES operations receives attention in Reference [10], which pioneers a carbon-constrained energy exchange mechanism. This protocol facilitates industrial surplus energy spot markets and strategic storage deployment, achieving documented reductions in both carbon footprints and economic losses across case implementations. Extending this line of inquiry, Reference [11] incorporates lifecycle emission accounting into its tiered trading architecture, revealing through techno-economic analysis that equipment-specific modeling and hydrogen admixture strategies can yield 18%–22% additional emission abatement. Cross-system coordination emerges as a research frontier in Reference [12], which conceptualizes an electric-carbon nexus framework for multi-district integrated energy systems (MDIES) through federated market design. By exploiting regional carbon pricing differentials, this model enables inter-jurisdictional quota arbitrage and collective cost minimization. These collective advances underscore three critical success factors: 1) multi-vector energy synergies, 2) adaptive demand-side management, and 3) spatially optimized energy allocation protocols. Recent investigations explore collaborative governance models. Reference [13] devises a cooperative planning mechanism with Shapley value-based cost apportionment for shared storage infrastructure, while Reference [14] demonstrates a distributed renewable-driven system optimized through metaheuristic algorithms. To address multi-zone coordination challenges, Reference [15] establishes a Nash bargaining-based cooperative game model incorporating hydrogen energy trading. Concurrently, Reference [16] pioneers a tri-objective optimization framework integrating power-to-gas conversion and multimodal demand response, achieving simultaneous minimization of operational costs, emissions, and exergy losses.

In summary, the existing research has the following gaps: 1) inadequate hydrogen energy integration in current system architectures, 2) overreliance on static carbon pricing mechanisms with limited dynamic incentives, and 3) predominant focus on conventional energy vectors (electricity/heat/gas) at the expense of emerging alternatives. Current carbon reduction strategies, predominantly employing rigid tiered taxation models, prove deficient in both flexibility and incentive compatibility—exhibiting punitive characteristics while lacking reward mechanisms. This study therefore proposes an adaptive carbon-market-embedded energy coordination model, designed to reconcile evolving energy portfolios with complex market dynamics through hybrid incentive structures and cross-vector synergies.

In operational contexts, PIES scheduling optimization is frequently subject to multifaceted interdependencies among system variables, rendering the identification of universally optimal solutions particularly challenging. This complexity necessitates advanced optimization techniques with robust computational efficiency to derive Pareto-optimal configurations within feasible operational boundaries. Intelligent metaheuristic algorithms have emerged as viable computational tools for navigating such multidimensional solution spaces. Reference [17] proposes a hybrid metaheuristic framework combining an augmented Coyote Optimization Algorithm with quadratic programming, implementing a bi-level optimization architecture grounded in Stackelberg game-theoretic principles for coordinated energy dispatch in PIES. This methodological innovation demonstrates enhanced convergence properties and computational tractability when handling non-convex, multi-objective optimization problems characteristic of real-world energy system operations. Reference [18] introduces an optimal scheduling method for complex integrated energy systems, utilizing a heuristic algorithm to optimize energy, economic, and environmental metrics while refining the operational plan. The method improves the convergence rate of the heuristic algorithm by incorporating k-means clustering along with box plot analysis to set its initial conditions. Reference [19] implements a hybrid Slime Mold-Artificial Bee Colony (SMABC) algorithm for operational optimization of multi-vector energy systems integrating electricity-gas-heat-cooling networks with renewable generation, power-to-hydrogen (P2H) conversion, power-to-gas (P2G), hydrogen fuel cells, and thermal recovery infrastructure. Comparative simulations demonstrate the SMABC's superiority over conventional Particle Swarm Optimization (PSO) and standalone Slime Mold algorithms, achieving 12%–15% cost reductions and 18%–22% lower carbon intensity in techno-economic evaluations. Reference [20] proposes a novel chaotic artificial hummingbird algorithm for low-carbon dispatch optimization, resolving the trilemma of operational cost minimization (14% improvement), emission control (27% reduction), and renewable utilization maximization (89% penetration rate). This bio-inspired metaheuristic demonstrates enhanced convergence characteristics and Pareto front distribution compared to legacy methods, effectively bridging the gap between economic dispatch protocols and decarbonization objectives aligned with carbon peaking/neutrality timelines.

In conclusion, while significant progress has been made in optimizing the scheduling of PIES in the current literature, several challenges persist. 1) The existing tiered carbon trading framework provides insufficient pressure on emission constraints, indicating a need for enhancements that can better encourage enterprises to achieve voluntary emission reductions and improve efficiency. 2) Traditional intelligent optimization algorithms often become trapped in local optima during objective optimization, demonstrating weak global search capabilities and slow convergence rates, thereby underscoring the necessity for newer optimization techniques. 3) Despite advancements in Combined Heat and Power (CHP) systems and Power-to-Gas (P2G) technologies that have increased the flexibility of integrating wind and solar energy into PIES, economic feasibility and low-carbon performance still possess notable shortcomings. 4) As the economy and society evolve, the variety of energy sources within PIES continues to grow. Consequently, conventional electric-thermal complementary PIES fail to meet current demands. With the widespread adoption of hydrogen energy, it is crucial to explore optimization scheduling strategies for PIES that incorporate diverse energy sources, including hydrogen.

This paper presents a reward-and-punishment optimization strategy aimed at balancing energy generation, supply, and consumption within integrated parks, focusing on the integration of Power-to-Gas (P2G) and Carbon Capture and Storage (CCS) technologies alongside hydrogen use. Initially, we enhance the traditional tiered carbon quota trading approach by incorporating a reward-and-punishment coefficient, leading to the development of an improved tiered carbon trading model. We then consider the coordinated operation of P2G and CCS systems, Combined Heat and Power (CHP) systems, various energy storage technologies, hydrogen utilization, and renewable energy generation, resulting in a PIES that encompasses four types of energy: electricity, heat, gas, and hydrogen. For intra-day ultra-short-term load forecasting within the PIES, we utilize the adaptive noise Complete Ensemble Empirical Mode Decomposition with Adaptive Noise (CEEMDAN) in conjunction with a convolutional neural network (CNN) integrated with a Long-Term and Short-Term Memory neural network (LSTM) prediction model (CEEMDAN-CNN-LSTM) to ensure the equilibrium of generation, supply, and demand. Next, we formulate an optimization scheduling model aimed at minimizing the total cost of the PIES. We also introduce the Shuffled Barebones Optimization Algorithm (SBOA) and demonstrate its advantages in optimization efficiency, convergence speed, and overall performance compared to leading intelligent optimization algorithms using the CEC2005 benchmark functions. Finally, we evaluate the model under five distinct scenarios, confirming the effectiveness of the proposed strategy through the obtained computational results.

The innovations detailed in this paper can be categorized as follows: 1) Innovative Optimization Strategy: A reward-and-punishment framework has been introduced to effectively balance energy generation, supply, and consumption within integrated parks. 2) Improved Carbon Trading Framework: The conventional tiered carbon quota trading system has been enhanced by integrating a reward-and-punishment coefficient, leading to a more refined carbon trading model. 3) Multiple Energy Source Integration: A PIES has been developed to incorporate electricity, heat, gas, and hydrogen through the synergy of P2G and CCS technologies. 4) Ultra-Short-Term Load Forecasting: The CEEMDAN-CNN-LSTM model has been employed for intra-day ultra-short-term load forecasting to ensure balance in energy generation, supply, and consumption. 5) Cost Minimization Framework: An optimization scheduling model has been devised aimed at minimizing the overall costs of the PIES, providing a theoretical foundation for improving economic efficiency. 6) SBOA Implementation and Performance: The implementation of the SBOA is highlighted, demonstrating its superior optimization capabilities, rapid convergence, and enhanced operational efficiency. 7) Validation Across Various Scenarios: The model has been assessed under five distinct scenarios to confirm the effectiveness of the proposed strategy, thereby enhancing its applicability in practical settings.

2 Basic Structure of PIES

The PIES framework developed in this research is depicted in Fig. 1. On the energy generation side, it features photovoltaic (PV) systems, Carbon Capture and Storage (CCS) units, Power-to-Gas (P2G) devices, gas turbines (GT), gas boilers (GB), waste heat boilers (WHB), and Organic Rankine Cycle (ORC) systems. The energy supply side includes the electricity grid, gas grid, hydrogen network, energy storage (ES), hydrogen fuel cells (HFC), gas storage (GasS), thermal storage (hS), and hydrogen storage. Meanwhile, the energy demand side encompasses electricity, heat, and gas demands. The integration of GT, WHB, ORC, and HFC creates a Combined Heat and Power (CHP) system. CCS works with P2G by providing CO_2, while HFC and GT supply thermal energy to the ORC, allowing for flexible thermal and electrical responses on the supply side. Actual carbon emissions from each device in the PIES are traded in the carbon market along with their associated carbon allowances.

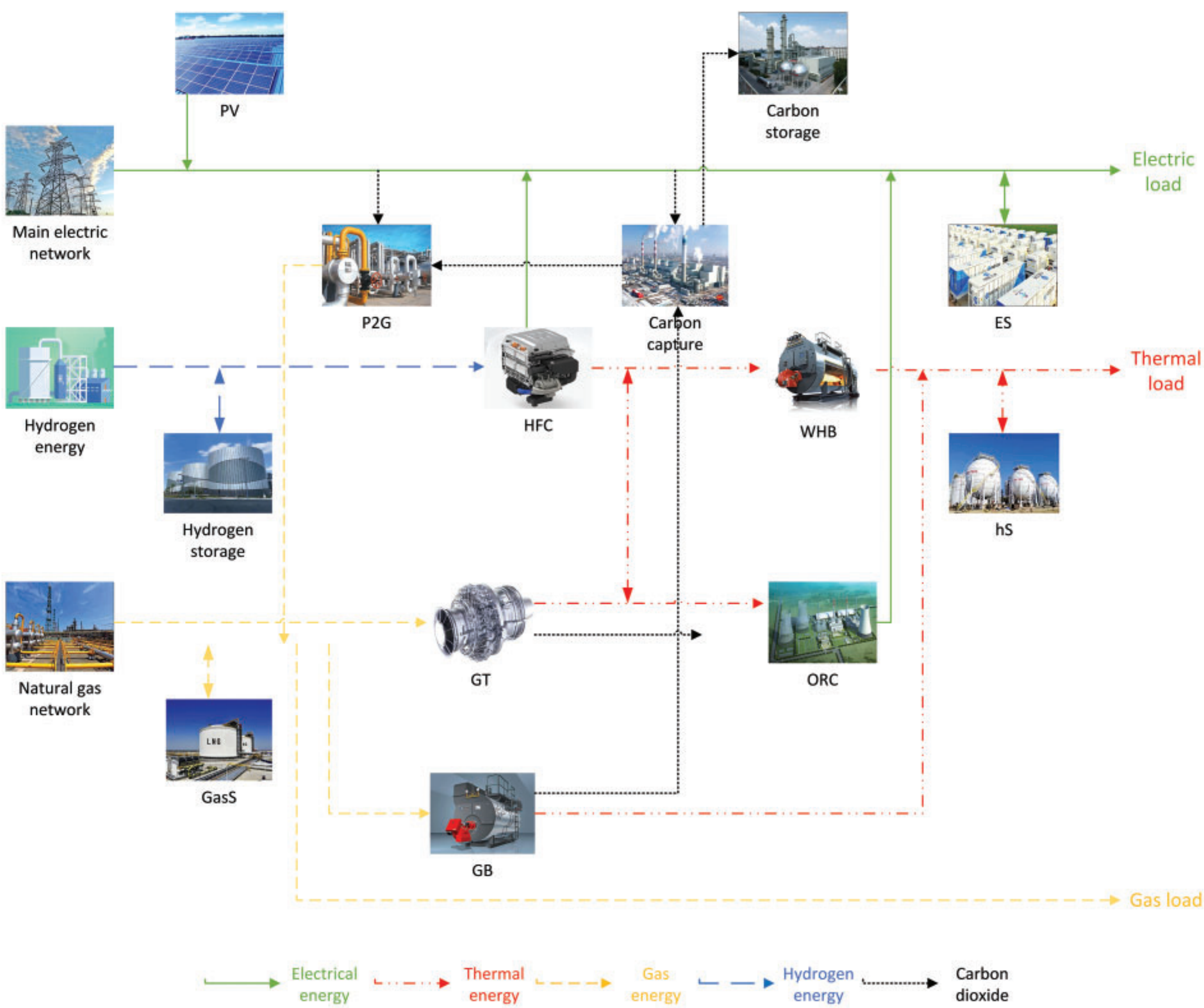

Figure 1: Internal structure of PIES

3 Real-Time Supply and Demand Balancing Strategy in Industrial Parks Considering a Reward-Punishment Carbon Trading Mechanism

3.1 Reward-Punishment Carbon Trading Mechanism Model

3.1.1 Distribution Mechanism of PIES Carbon Emission Quotas

The reward-punishment carbon trading mechanism enhances the traditional tiered carbon trading system by incorporating a reward-punishment coefficient. In this model, businesses not only buy or sell carbon quotas based on the gap between their allocated free quotas and actual emissions, but they also participate in a system of rewards and penalties linked to their emissions. Specifically, enterprises with carbon emissions below their allocated quotas can receive financial incentives. In contrast, if emissions exceed the allocated limits, the businesses face penalty fees. This incentive mechanism serves to further encourage companies to reduce their carbon emissions actively. The specific process is represented in Fig. 2.

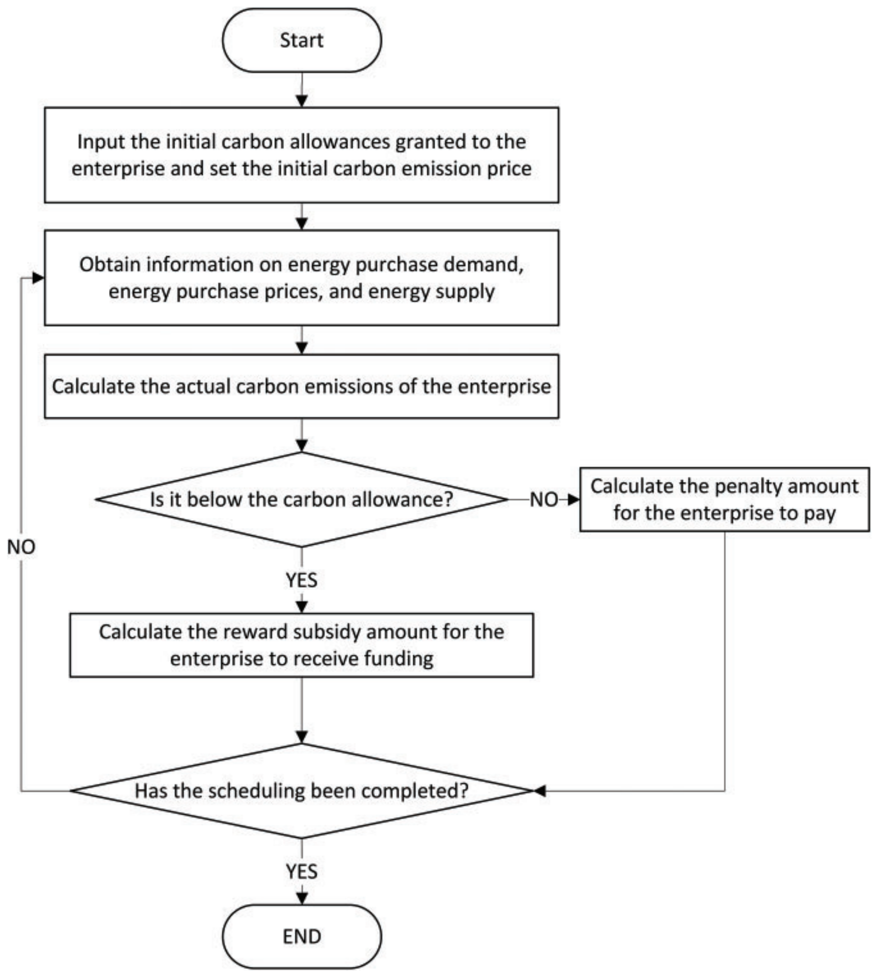

Figure 2: Flow of reward-penalty ladder carbon trading mechanism

3.1.2 Initial Allocation Model for PIES Carbon Emission Rights

In the context of PIES, carbon emission sources include emissions from purchasing electricity from coal-fired power plants, gas boiler emissions, gas turbine emissions, and waste heat boiler emissions. The initial allocation model for carbon emissions is as follows:

$$\begin{cases} E_{PIES} = E_{buy}^{TE} + E_{GT} + E_{GB} \\ E_{buy}^{TE} = \gamma_e \sum_{t=1}^{T} P_{buy}^{TE}(t) \\ E_{GT} = \gamma_h \sum_{t=1}^{T} \left(\sigma_{e,h} P_{GT}^{e}(\mathrm{t}) + P_{GT}^{h}(t) \right) \\ E_{GB} = \gamma_h \sum_{t=1}^{T} P_{GB}(t) \end{cases} \tag{1}$$

where: E_{PIES}, E_{buy}^{TE}, E_{GT}, and E_{GB} denote the carbon emission quotas associated with the PIES, electricity acquired from coal-fired power plants, emissions from gas turbines, and emissions from gas boilers, respectively. γ_e and γ_h represent the allocated quotas of free carbon emission rights per unit of electricity and heat produced, respectively. $\sigma_{e,h}$ is the conversion coefficient that relates electrical output from gas turbines to heat output. $P_{buy}^{TE}(t)$ indicates the power purchased from the higher-level grid at time *t*. Both $P_{GT}^{e}(t)$ and $P_{GT}^{h}(t)$ represent the electricity and heat produced by the gas turbine at time *t*. $P_{GB}(t)$ refers to the heat produced by the gas boiler during the specified time period *t*. Lastly, T represents the scheduling period.

3.1.3 Actual Carbon Emission Model of PIES

In the process of converting electricity to gas within the system, a portion of the CO_2 will be consumed, while CCS technology can capture a significant amount of CO_2. Therefore, the revised actual carbon emission model is as follows:

$$\begin{cases} \mathrm{E}_{\mathrm{PIES}}^{'} = \mathrm{E}_{\mathrm{buy}}^{\mathrm{TE}'} + \mathrm{E}_{\mathrm{GT}}^{'} + \mathrm{E}_{\mathrm{GB}}^{'} - \mathrm{E}_{\mathrm{CC,a}} \\ \mathrm{E}_{\mathrm{buy}}^{\mathrm{TE}} = \sum_{\mathrm{t}=1}^{\mathrm{T}} \left(\mathrm{a}_1 + \mathrm{b}_1 \mathrm{P}_{\mathrm{buy}}^{\mathrm{TE}}(\mathrm{t}) + \mathrm{c}_1 \mathrm{P}_{\mathrm{buy}}^{\mathrm{TE}}(\mathrm{t})^2 \right) \\ \mathrm{E}_{\mathrm{GT}} = \gamma_{\mathrm{h}}^{*} \sum_{\mathrm{t}=1}^{\mathrm{T}} \left(\sigma_{\mathrm{e,h}} \mathrm{P}_{\mathrm{GT}}^{\mathrm{e}}(\mathrm{t}) + \mathrm{P}_{\mathrm{GT}}^{\mathrm{h}}(\mathrm{t}) \right) \\ \mathrm{E}_{\mathrm{GB}} = \gamma_{\mathrm{h}}^{*} \sum_{\mathrm{t}=1}^{\mathrm{T}} \mathrm{P}_{\mathrm{GB}}(\mathrm{t}) \\ \mathrm{E}_{\mathrm{CC,a}} = \sum_{\mathrm{t}=1}^{\mathrm{T}} \mathrm{E}_{\mathrm{CC}}(\mathrm{t}) \end{cases} \tag{2}$$

where: $E_{PIES}^{'}$ represents the actual carbon emissions from PIES; $E_{buy}^{TE'}$ denotes the actual carbon emissions from thermal power purchased from the upper-level grid; $E_{GT}^{'}$ indicates the actual carbon emissions resulting from gas turbines; and $E_{GB}^{'}$ signifies the actual carbon emissions from gas boilers. The parameters a_1, b_1, and c_1 are employed to compute the actual carbon emissions of thermal power units. γ_h^{*} represents the actual carbon emissions per unit of thermal power generated, while $E_{CC,a}$ refers to the total amount of carbon captured during the dispatch period, and $E_{CC}(t)$ represents the carbon capture and storage executed by CCS during the time frame *t*.

3.1.4 PIES Incentive-Based Tiered Carbon Trading Cost Model

To further reduce carbon emissions within the system and stimulate the emission reduction potential of energy enterprises, an incentive-based tiered carbon trading cost mathematical model has been established, which can be expressed as:

$$f_{CO_2}^{trade} = \begin{cases} -c\left(1+2\mu\right)\left(E_{PIES} - l - E_{PIES}^{'}\right), E_{PIES}^{'} - E_{PIES} < -l \\ -c\left(1+2\mu\right)l - c\left(1+\mu\right)\left(E_{PIES} - E_{PIES}^{'}\right), -l \leq E_{PIES}^{'} - E_{PIES} \leq 0 \\ c\left(E_{PIES}^{'} - E_{PIES}\right), 0 < E_{PIES}^{'} - E_{PIES} \leq l \\ ch + c\left(1+\lambda\right)\left(E_{PIES}^{'} - E_{PIES} - l\right), l < E_{PIES}^{'} - E_{PIES} \leq 2l \\ c\left(2+\lambda\right)l + c\left(1+2\lambda\right)\left(E_{PIES}^{'} - E_{PIES} - 2l\right), 2l < E_{PIES}^{'} - E_{PIES} \leq 3l \\ c\left(3+3\lambda\right)l + c\left(1+3\lambda\right)\left(E_{PIES}^{'} - E_{PIES} - 3l\right), E_{PIES}^{'} - E_{PIES} > 3l \end{cases} \tag{3}$$

where: $f_{CO_2}^{trade}$ represents the incentive-based tiered carbon trading cost for PIES; c denotes the baseline carbon trading price; l refers to the interval length of carbon trading volume; and μ and λ represent the incentive and penalty coefficients, respectively.

3.2 Real-Time Supply and Demand Balancing Model for the Park

3.2.1 Ultra-Short-Term Prediction Method for Electric, Thermal, Gas, and Hydrogen Loads

To maintain a stable energy supply within the PIES, it is essential to predict electric, thermal, gas, and hydrogen loads for the upcoming scheduling period before each dispatch cycle. This forecast provides insights into energy demand on the consumption side, allowing for the reverse engineering of power output schemes for equipment on the supply side as well as the identification of optimal dispatch strategies. Currently, there are established techniques for ultra-short-term load forecasting, and thus this paper will not focus in detail on the modeling methods. Instead, we will employ the CEEMDAN-CNN-LSTM method based on density clustering, as outlined in reference [21], for ultra-short-term predictions of electric, thermal, gas, and hydrogen loads.

3.2.2 Supply and Demand Side Balancing Response Model

(1) Photovoltaic Generation Unit Model

$$P_t^{PV} = \begin{cases} S_{PV}\dfrac{I_t}{I}, 0 \leq I_t < I \\ S_{PV}, I_t \geq I \end{cases} \tag{4}$$

where: P_t^{PV} represents the photovoltaic power output during time period t; S_{PV} denotes the capacity of the photovoltaic unit; I_t indicates the solar irradiance during time period t; and I is the rated solar irradiance.

Thus, the photovoltaic generation during time period t can be expressed as:

$$Q_t^{PV} = P_t^{PV}\Delta t \tag{5}$$

where: Q_t^{PV} denotes the photovoltaic energy output during time period t, and Δt represents the time interval for that period.

(2) Hydrogen Fuel Cell Device Model

$$\begin{cases} P_{HFC}^{e}(t) = \eta_{HFC}^{e} P_{HFC}^{H_2}(t) \\ P_{HFC}^{h}(t) = \eta_{HFC}^{h} P_{HFC}^{H_2}(t) \\ P_{H_2,HFC}^{min} \le P_{HFC}^{H_2}(t) \le P_{H_2,HFC}^{max} \\ \Delta P_{H_2,HFC}^{min} \le P_{HFC}^{H_2}(t+1) - P_{HFC}^{H_2}(t) \le \Delta P_{H_2,HFC}^{max} \end{cases} \tag{6}$$

where: $P_{HFC}^{H_2}(t)$ represents the hydrogen power input to the HFC at time t; $P_{HFC}^{e}(t)$ and $P_{HFC}^{h}(t)$ indicate the electrical and thermal power outputs of the HFC at time t, respectively. η_{HFC}^{e} and η_{HFC}^{h} refer to the generation and heating efficiencies of the HFC device. $P_{H_2,HFC}^{min}$ and $P_{H_2,HFC}^{max}$ denote the minimum and maximum limits of the HFC input power, while $\Delta P_{H_2,HFC}^{min}$ and $\Delta P_{H_2,HFC}^{max}$ represent the minimum and maximum limits of the HFC ramp-up power.

(3) Gas Turbine Model

$$\begin{cases} P_{GT}^{e}(t) = \eta_{GT}^{e} P_{GT}^{Gas}(t) \\ P_{GT}^{h}(t) = \eta_{GT}^{h} P_{GT}^{Gas}(t) \\ P_{Gas,GT}^{min} \le P_{GT}^{Gas}(t) \le P_{Gas,GT}^{max} \\ \Delta P_{Gas,GT}^{min} \le P_{GT}^{Gas}(t+1) - P_{GT}^{Gas}(t) \le \Delta P_{Gas,GT}^{max} \end{cases} \tag{7}$$

where: $P_{GT}^{Gas}(t)$ indicates the natural gas power input to the GT during time period t; $P_{GT}^{i}(t)$ denotes the power output of the GT for the i-th type of energy during the same time frame; η_{GT}^{i} represents the efficiency of the GT in producing the i-th energy type; $P_{Gas,GT}^{max}$ and $P_{Gas,GT}^{min}$ specify the upper and lower limits of the GT's power input, respectively; and $\Delta P_{Gas,GT}^{max}$ and $\Delta P_{Gas,GT}^{min}$ indicate the maximum and minimum ramp-up power limits of the GT, respectively.

(4) Combined Heat and Power System Model

The electrical power generated by the HFC and GT meets the electrical load requirements, while some of the thermal power produced is directed to the WHB to satisfy heating needs. Any surplus thermal power is diverted to the ORC for waste heat recovery and electricity generation, which is then supplied to the electrical load. This integration of HFC, GT, WHB, and ORC forms a CHP system capable of adapting to both heat and electricity supply demands. The model can be represented by the following equation:

$$\begin{cases} P_{HFC}^{h}(t) = p_{HFC,WHB}^{h}(t) + P_{HFC,ORC}^{h}(t) \\ P_{GT}^{h}(t) = P_{GT,WHB}^{h}(t) + P_{GT,ORC}^{h}(t) \\ P_{WHB}^{h,in}(t) = P_{HFC,WHB}^{h}(t) + P_{GT,WHB}^{h}(t) \\ P_{ORC}^{h,in}(t) = P_{HFC,ORC}^{h}(t) + P_{GT,ORC}^{h}(t) \\ P_{WHB}^{h,out}(t) = \eta_{WHB} P_{WHB}^{h,in}(t) \\ P_{ORC}^{e,out}(t) = \eta_{ORC} P_{ORC}^{h,in}(t) \\ P_{WHB}^{h,min} \le P_{WHB}^{h,in} \le P_{WHB}^{h,max} \\ P_{ORC}^{h,min} \le P_{ORC}^{h,in} \le P_{ORC}^{h,max} \\ \Delta P_{WHB}^{h,min} \le P_{WHB}^{h,in}(t+1) - P_{WHB}^{h,in}(t) \le \Delta P_{WHB}^{h,max} \\ \Delta P_{ORC}^{h,min} \le P_{ORC}^{h,in}(t+1) - P_{ORC}^{h,in}(t) \le \Delta P_{ORC}^{h,max} \end{cases} \tag{8}$$

where: $p^{h}_{HFC,WHB}(t)$ and $P^{h}_{HFC,ORC}(t)$ represent the thermal power output from the HFC to the WHB and ORC at time t, respectively. $P^{h}_{GT,WHB}(t)$ and $P^{h}_{GT,ORC}(t)$ denote the thermal power output from the GT to the WHB and ORC at the same time. $P^{h,in}_{WHB}(t)$ and $P^{h,in}_{ORC}(t)$ indicate the input thermal power to the WHB and ORC during t. $P^{h,out}_{WHB}(t)$ represents the output thermal power from the WHB at time t, while $P^{e,out}_{ORC}(t)$ indicates the output electrical power from the ORC at that moment. η_{WHB} and η_{ORC} are the conversion efficiencies for the WHB and ORC, respectively. $P^{h,max}_{WHB}$ and $P^{h,min}_{WHB}$ denote the maximum and minimum limits of input thermal power to the WHB, while $P^{h,max}_{ORC}$ and $P^{h,min}_{ORC}$ indicate the corresponding limits for the ORC.

The final output of electrical and thermal power from the CHP system is as follows:

$$\begin{cases} P^{e}_{CHP}(t) = P^{e}_{HFC}(t) + P^{e}_{GT}(t) + P^{e,out}_{ORC}(t) \\ P^{h}_{CHP}(t) = P^{h,out}_{WHB}(t) \end{cases} \tag{9}$$

where: $P^{e}_{CHP}(t)$ and $P^{h}_{CHP}(t)$ represent the electrical and thermal power outputs of the CHP system, respectively.

(5) CCS Model

The CCS system mainly comprises two key stages: carbon capture and carbon storage. The captured CO_2 is partly transported through pipelines to P2G facilities for recycling, while the rest is stored using a CO_2 compressor. Energy consumption during the capture process can be divided into fixed and operational categories. Fixed energy consumption results from alterations caused by integrating CCS into traditional coal and gas unit frameworks, remaining constant regardless of CCS's operational status, and is primarily reflected in decreased power generation efficiency. In contrast, operational energy consumption stems from the thermal energy required for CO_2 regeneration and the electrical energy used during compression. This component constitutes the majority of the total energy consumption of CCS and is closely tied to its operational conditions. The specific expressions are as follows:

$$\begin{cases} P_{CCUS}(t) = P^{r}_{CCUS}(t) + P^{s}_{CCUS} \\ P^{r}_{CCUS}(t) = \lambda_{GE}\eta_{C}e_{G}P_{G}(t) \\ E_{CC}(t) = \eta_{C}e_{G}P_{G}(t) \\ 0 \le P_{CCUS}(t) \le P^{max}_{CCUS} \end{cases} \tag{10}$$

where: $P_{CCUS}(t)$ represents the total power of the CCS at time t; $P^{r}_{CCUS}(t)$ denotes the operational energy consumption of the CCS during this time; $P^{s}_{CCUS}(t)$ refers to the fixed energy consumption of the CCS, treated as a constant; $P_{G}(t)$ signifies the power output from coal or gas units at t; e_G is the carbon emission intensity per unit of electricity produced; η_c indicates the carbon capture efficiency of the CCS, assumed to be 90% in this analysis; λ_{GE} represents the electrical power consumption per unit of CO_2 captured; and $E_{CC}(t)$ denotes the quantity of CO_2 captured at time t. Additionally, P^{max}_{CCUS} defines the maximum operational power limit for the CCS.

(6) Two-Stage P2G Model

The P2G technology transforms electricity produced from wind and solar energy into storable natural gas, which can be provided to natural gas-consuming devices within the PIES as needed. The P2G process consists of two primary stages: electrolysis to produce hydrogen and methanation. In the methanation phase, the volume of CO_2 utilized matches the volume of natural gas generated. The specific equation is as follows:

$$\begin{cases} P_{P2G}^{Gas}(t) = \eta_{P2G} P_{P2G}^{e}(t) \\ V_{CO_2}(t) = V_{Gas}(t) = 3.6 P_{P2G}^{Gas}(t)/H_g \\ E_{P2G}^{CO_2}(t) = \rho_{CO_2} V_{CO_2}(t) \end{cases} \tag{11}$$

where: $P_{P2G}^{e}(t)$ represents the electrical power input to the P2G system during time period t; $P_{P2G}^{Gas}(t)$ indicates the output power of natural gas from the P2G system in the same timeframe; η_{P2G} denotes the conversion efficiency of the P2G process; $V_{CO_2}(t)$ and $V_{Gas}(t)$ refer to the volumes of CO_2 captured and natural gas produced by the P2G system during time period t, respectively; H_g is the calorific value of natural gas, which is 39 MJ/m^3; and $E_{P2G}^{CO_2}$ signifies the mass of CO_2 absorbed by the P2G system during time period t, while ρ_{CO_2} represents the density of CO_2.

3.2.3 Energy Consumption Side Balance Response Model

In the PIES system, the demand response loads comprise fixed loads, transferable loads, and substitute loads.

$$P_{k,load}(t) = P_{k,load}^{s}(t) + P_{k,load}^{p}(t) + P_{k,load}^{c}(t) \tag{12}$$

where: k indicates the type of load; $P_{k,load}(t)$ represents the power of the k-th load at time t; $P_{k,load}^{s}(t)$, $P_{k,load}^{p}(t)$, and $P_{k,load}^{c}(t)$ correspond to the fixed load, transferable load, and substitute load of the k-th type at time t, respectively.

In summary, the Demand Response (DR) model can adjust energy demand through various response mechanisms, as detailed below:

$$P_{k,load}^{*} = P_{k,load}(t) + P_{k,load}(t) = P_{k,load}(t) + P_{k,load}^{p}(t) + P_{k,load}^{c}(t) \tag{13}$$

where: $P_{k,load}^{*}$ represents the power of the k-th load during the t-th period after participating in balanced demand response.

4 Punishment and Reward-Based Ladder Carbon Trading: A Supply-Demand Balance Model for Parks Based on Vulture Optimization Algorithm

4.1 Objective Function

The goal of optimization is to minimize the total operational cost F of the PIES. This cost encompasses the energy purchase expense f_{buy}, carbon cost f_{CO_2}, demand response compensation cost f_{DR}, and curtailed energy penalty cost f_{cur}, as shown in the following equation:

$$F = \min\left(f_{buy} + f_{CO_2} + f_{DR} + f_{cur}\right) \tag{14}$$

4.1.1 Energy Purchase Cost

The energy purchase cost f_{buy} is comprised of the electricity purchase cost f_{buy}^{e}, gas purchase cost f_{buy}^{Gas}, and hydrogen purchase cost $f_{buy}^{H_2}$. The specific calculation methods are as follows:

$$\begin{cases} f_{buy} = f_{buy}^{e} + f_{buy}^{Gas} + f_{buy}^{H_2} \\ f_{buy}^{e} = \sum_{t=1}^{T} C_e(t) P_{buy}^{e}(t) \\ f_{buy}^{Gas} = \sum_{t=1}^{T} C_{Gas}(t) P_{buy}^{Gas}(t) \\ f_{buy}^{H_2} = \sum_{t=1}^{T} C_{h_2}(t) P_{buy}^{H_2}(t) \end{cases} \tag{15}$$

where: $P_{buy}^{i}(t)$ denotes the power bought for the i-th energy type in time period t; $C_e(t)$ is the unit price of electricity at time t; $C_{Gas}(t)$ is the unit price of gas at time t; and $C_{h_2}(t)$ represents the unit price of hydrogen at time t.

4.1.2 Carbon Cost

The carbon cost f_{CO_2} encompasses the tiered carbon trading cost $f_{CO_2}^{trade}$, carbon capture cost $f_{CO_2}^{cc}$, and carbon storage cost $f_{CO_2}^{cs}$. CCS technology requires considerable energy for the CO_2 capture process. If this energy were redirected to satisfy demand-side loads, it could generate revenue from electricity sales; therefore, the foregone revenue also adds to the carbon capture cost. Moreover, the carbon storage process involves expenditures for compression, transportation, and storage. The specific calculations are as follows:

$$\begin{cases} f_{CO_2}^{cc} = \sum_{t=1}^{T} C_e(t) P_{CCS}(t) \\ f_{CO_2}^{cs} = \sum_{t=1}^{T} C_{cs}\left(E_{CC}(t) - E_{P2G}^{CO_2}(t)\right) \end{cases} \tag{16}$$

where: C_{cs} represents the coefficient of carbon storage cost.

4.1.3 Demand Response Compensation Cost

DR compensation cost f_{DR} is expressed as follows:

$$\begin{gathered} f_{DR} = \sum_{t=1}^{T}((\lambda_p(\left|P_{e,Load}^{p}(t)\right| + \left|P_{h,Load}^{p}(t)\right| + \left|P_{Gas,Load}^{p}(t)\right|) + \\ \lambda_c\left(\left|P_{e,Load}^{c}(t)\right| + \left|P_{h,Load}^{c}(t)\right| + \left|P_{Gas,Load}^{c}(t)\right|\right)) \end{gathered} \tag{17}$$

where: λ_p and λ_c represent the unit compensation coefficients for transferable load and substitutable load, respectively.

4.1.4 Curtailment Penalty Costs

Using electricity produced by photovoltaic and wind power can improve the integration of renewable energy, supporting the low-carbon transition of PIES. If renewable energy generation is not utilized, a curtailment penalty cost will be incurred.

$$C_{cur} = \sum_{t=1}^{T} c_{PV} P_{CPV}(t) \tag{18}$$

where: $P_{CPV}(t)$ represents the curtailed solar power at time t; c_{PV} denotes the penalty coefficients for solar curtailment.

4.2 Constraints

4.2.1 Ultra-Short-Term Load Forecasting Balance Constraint

According to the range of load margin safety operation constraint index mentioned in reference [22], we take 5% as the margin and model it as follows:

$$\begin{cases} P_e \leq O_{PV} + O_{buy}^{e} + O_{H_2} + O_{HFC} + O_{CHP}^{e} + O_{ES}^{cha} - O_{ES}^{dis} \leq 1.05P_e \\ P_h \leq O_{GB} + O_{CHP}^{h} + O_{ORC} + O_{hS}^{cha} - O_{hS}^{dis} \leq 1.05P_h \\ P_{Gas} \leq O_{Gas} + O_{P2G} + O_{GasS}^{cha} - O_{GasS}^{dis} \leq 1.05P_{Gas} \end{cases} \tag{19}$$

where: P_e, P_h, and P_{Gas} represent the forecasted demand for electrical, thermal, and gas loads, respectively. The terms O_{PV}, O_{buy}^{e}, O_{H_2}, O_{HFC}, and O_{CHP}^{e} indicate the electrical output from photovoltaic units, the grid, hydrogen energy, hydrogen fuel cells, and CHP systems, respectively. Additionally, O_{GB}, O_{CHP}^{h}, and O_{ORC} denote the thermal output from gas boilers, CHP systems, and ORC systems, respectively. Finally, O_{Gas} and O_{P2G} represent the gas output from the gas network and the power-to-gas conversion process, respectively.

4.2.2 Energy Storage Operational Constraints

This study utilizes a generalized model of energy storage systems to model the storage of electricity, heat, gas, and hydrogen. For specific details, please refer to reference [23].

4.2.3 CHP Operational Constraints

The operational constraints associated with the components within the CHP system, including HFC, GT, ORC, and WHB, are detailed in Section 3.2.2.

4.2.4 GB Operational Constraints

$$\begin{cases} P_{GB}^{h}(t) = \varphi_{GB} P_{GB}^{Gas}(t) \\ P_{GB,Gas}^{min} \leq P_{GB}^{Gas}(t) \leq P_{GB,Gas}^{max} \\ \triangle P_{GB,Gas}^{min} \leq P_{GB,Gas}(t+1) - P_{GB,Gas}(t) \leq \triangle P_{GB,Gas}^{max} \end{cases} \tag{20}$$

where: φ_{GB} signifies the energy conversion efficiency of the GB; $P_{GB,Gas}(t)$ denotes the natural gas power input to the GB during time period t; $P_{GB,Gas}^{min}$ and $P_{GB,Gas}^{max}$ specify the operational limits for the power input to the GB; $\Delta P_{GB,Gas}^{min}$ and $\Delta P_{GB,Gas}^{max}$ set the ramping constraints for the GB.

4.2.5 Power Balance Constraints

(1) Electric Power Balance Constraints

Assuming no electricity is sold to the higher-level grid, the electric power balance is as follows:

$$\begin{cases} P_{buy}^{e}(t) + P_{CHP}^{e}(t) + P_{PV}(t) = P_{load}^{e}(t) + P_{P2G}^{e}(t) + P_{CCUS}(t) + P_{ES}^{cha}(t) - P_{ES}^{dis}(t) \\ 0 \le P_{buy}^{e}(t) \le P_{e,buy}^{max} \\ 0 \le P_{PV}(t) \le P_{PV}^{max} \end{cases} \tag{21}$$

where: P_{load}^{e} indicates the electric load during time period t; $P_{CCUS}(t)$ represents the total power of the CCS in this same period; $P_{ES}^{cha}(t)$ and $P_{ES}^{dis}(t)$ refer to the charging and discharging power of the energy storage system, respectively; $P_{e,buy}^{max}$ and P_{PV}^{max} define the maximum limits for electricity purchased from the grid and the output from solar power, respectively.

(2) Gas Power Balance Constraints

$$\begin{cases} P_{buy}^{Gas}(t) = P_{load}^{Gas}(t) - P_{P2G,Gas}(t) + P_{GasS}^{cha}(t) - P_{GasS}^{dis}(t) + P_{GB}^{Gas}(t) + P_{GT}^{Gas}(t) \\ 0 \le P_{buy}^{Gas}(t) \le P_{Gas,buy}^{max} \end{cases} \tag{22}$$

where: $P_{GasS}^{cha}(t)$ and $P_{GasS}^{dis}(t)$ indicate the power inputs and outputs of the natural gas storage system in time period t, respectively; $P_{P2G,Gas}(t)$ signifies the power output of the P2G system during this time; therefore, $P_{Gas,buy}^{max}$ establishes the upper limit for gas power purchases from the higher-level natural gas network.

(3) Thermal Power Balance Constraint

$$P_{CHP,h}(t) + P_{GB}^{h}(t) = P_{load}^{h}(t) + P_{hS}^{cha}(t) - P_{hS}^{dis}(t) \tag{23}$$

where: $P_{load}^{h}(t)$ represents the thermal load in the t-th time period, while $P_{hS}^{cha}(t)$ and $P_{hS}^{dis}(t)$ denote the input and output power of the thermal energy storage system during that period, respectively.

(4) Hydrogen Energy Balance Constraint

$$\begin{cases} P_{buy}^{H_2}(t) = P_{HFC}^{H_2}(t) + P_{H_2S}^{cha}(t) - P_{H_2S}^{dis}(t) \\ 0 \le P_{buy}^{H_2}(t) \le P_{H_2,buy}^{max} \end{cases} \tag{24}$$

where: $P_{buy}^{H_2}(t)$ represents the power used for purchasing hydrogen during time period t; $P_{HFC}^{H_2}(t)$ indicates the hydrogen power input to the HFC for the same time period; $P_{H_2S}^{cha}(t)$ and $P_{H_2S}^{dis}(t)$ refer to the charging and discharging power of the hydrogen storage system during period t, respectively. The maximum allowable hydrogen purchase power is also specified.

5 Model Solution Algorithm

5.1 Snake-Buzzard Optimization Algorithm

This study employs the novel Snake-Buzzard Optimization Algorithm (SBOA), a bio-inspired meta-heuristic developed by Fu et al. (2024) [24], designed to overcome three critical limitations in conventional optimization paradigms: 1) premature convergence in Gray Wolf Optimization (GWO) architectures, 2) inadequate local search precision and solution accuracy in Particle Swarm Optimization (PSO) implementations, and 3) constrained search space exploration with suboptimal convergence rates in Sparrow Search Algorithm (SSA) variants.

Biologically inspired by the survival mechanisms of the African snake-buzzard (*Circaetus pectoralis*), SBOA emulates this raptor's dual-phase hunting strategy through mathematical formalization: 1) Exploration Phase: Simulates serpentine predation patterns using Levy flight dynamics for global search optimization. 2) Exploitation Phase: Implements threat-avoidance pathfinding through gradient-aware local search operators.

The algorithm's population-based architecture represents solutions as predator positions in an n-dimensional search space, with iterative position updates governed by ecological adaptation rules. As demonstrated in Fig. 3, key behavioral components—including prey identification (fitness evaluation), territorial surveillance (constraint handling), and threat response (gradient descent avoidance)—are systematically mapped to optimization operators.

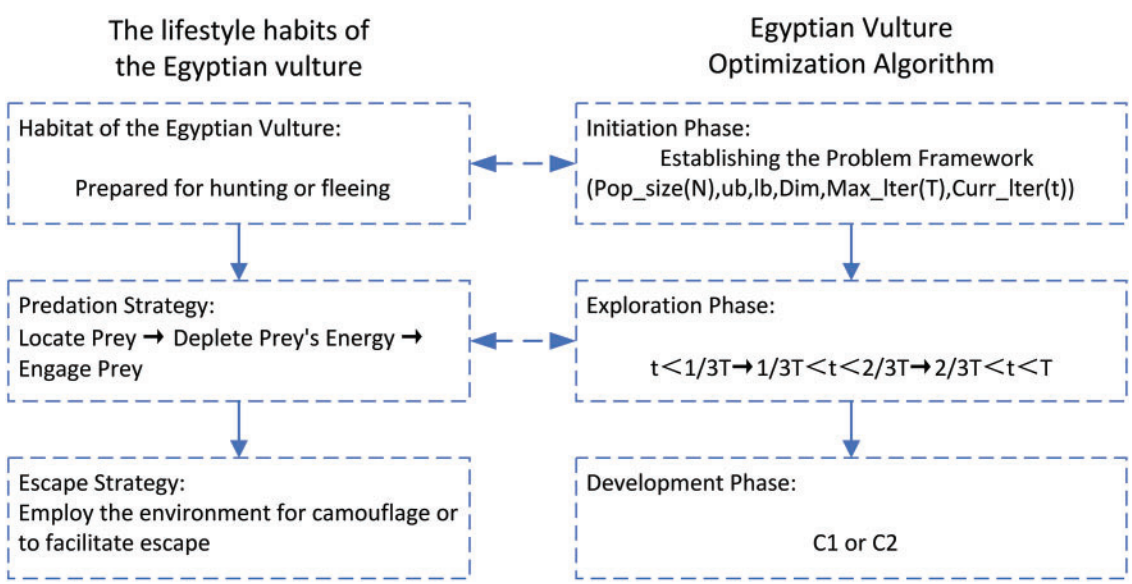

Figure 3: Correspondence between predation and escape behavior of Secretary bird and the SBOA

Native to sub-Saharan ecosystems including grasslands and riparian zones, the snake-buzzard's evolutionary adaptations provide unique biomimetic advantages for techno-economic optimization problems. The species' characteristic nest-site fidelity and thermal soaring behavior inform the algorithm's adaptive memory retention and landscape exploration mechanisms, respectively.

The specific formula is as follows:

First, the snake-buzzard population is initialized randomly:

$$X_{i,j} = lb_j + r \times \left(ub_j - lb_j\right), i = 1, 2, \cdots, N; j = 1, 2, \cdots, Dim \tag{25}$$

where: X_i denotes the position of the i-th snake-buzzard, while lb_j and ub_j represent the lower and upper bounds, respectively. The variable r is a random number between 0 and 1. Since the positions of the snake-buzzards and the corresponding objective function values are updated in each iteration, each member of the population is updated in two distinct phases based on the chosen hunting or escape strategy.

The hunting behavior of the snake-buzzard is divided into three phases: the first phase involves searching for prey, the second phase pertains to consuming the prey, and the third phase consists of attacking the prey. Based on biological statistics of the snake-buzzard's hunting stages and the duration of each phase, the entire hunting process is partitioned into three equal time intervals: t < 1/3T, 1/3T < t < 2/3T, and 2/3T < t < T, corresponding to the three phases of snake-buzzard predation.

In the first phase, a differential evolution strategy is employed. Differential evolution utilizes the differences among individuals to generate new solutions, thereby enhancing the algorithm's diversity and global search capability. By introducing differential mutation operations, this approach helps to avoid convergence to local optima. The specific representation is as follows:

$$While\ t < \frac{1}{3}T, x_{i,j}^{newP1} = x_{i,j} + \left(x_{random\_1} - x_{random\_2}\right) \times R_1 \tag{26}$$

$$X_i = \begin{cases} X_i^{new,P1}, if\ F_i^{new,P1} < F_i \\ X_i, else \end{cases} \tag{27}$$

where: t represents the current iteration number, T denotes the maximum number of iterations, x_i^{newP1} indicates the new position of the i-th vulture in the first phase, while x_{random_1} and x_{random_2} are random candidate solutions generated during the first phase of iteration. R_1 is an array of dimensions $1 \times Dim$ randomly generated from the interval [0, 1], where Dim refers to the dimensionality of the solution space. $x_{i,j}^{newP1}$ represents the value in the j-th dimension, and $F_i^{new,P1}$ indicates the accuracy of its objective function. In the second phase, Brownian motion (RB) is introduced to simulate the random movement of the vultures. During this phase, the vultures frequently pause to use their keen vision to locate the position of the prey. Here, the concept of x_{best} (the personal historical best position) is introduced, allowing the vultures to conduct local searches around their previously discovered optimal positions and better explore the surrounding solution space.

$$RB = randn\,(1, Dim) \tag{28}$$

$$While\ \frac{1}{3}T < t < \frac{2}{3}T, x_{i,j}^{newP1} = x_{best} + exp\left(\left(\frac{t}{T}\right) \wedge 4\right) \times (RB - 0.5) \times \left(x_{best} - x_{i,j}\right) \tag{29}$$

$$X_i = \begin{cases} X_i^{new,P1}, if\ F_i^{new,P1} < F_i \\ X_i, else \end{cases} \tag{30}$$

where: $randn(1, Dim)$ represents a $1 \times Dim$ array randomly generated from a standard normal distribution (mean 0, standard deviation 1), while x_{best} signifies the current optimal value.

In the third phase, a Levy flight strategy is introduced during the random search process to enhance the global search capability of the optimizer, thereby reducing the risk of the SBOA getting stuck in local solutions and improving the convergence accuracy of the algorithm. To increase the dynamism, adaptability, and flexibility of the SBOA during the optimization process, a better balance between exploration range and efficiency is achieved to avoid premature convergence, accelerate convergence, and enhance algorithm performance. To this end, the SBOA incorporates a nonlinear perturbation factor, represented by $\left(1 - \frac{t}{T}\right)^{\left(2 \times \frac{t}{T}\right)}$. The specific formulation is presented as follows:

$$While\ t > \frac{2}{3}T, x_{i,j}^{new\ P1} = x_{best} + \left(\left(1 - \frac{t}{T}\right) \wedge \left(2 \times \frac{t}{T}\right)\right) \times x_{i,j} \times RL \tag{31}$$

$$X_i = \begin{cases} X_i^{new,P1}, if\ F_i^{new,P1} < F_i \\ X_i, else \end{cases} \tag{32}$$

To enhance the performance of the algorithm, Levy flight is introduced, denoted as "RL."

$$RL = 0.5 \times Levy\left(Dim\right) \tag{33}$$

where: $Levy\left(Dim\right)$ denotes the $Levy$ flight distribution function, calculated as follows:

$$Levy\left(D\right) = s \times \frac{u \times \sigma}{|v|^{\frac{1}{\eta}}} \tag{34}$$

where: s is a fixed constant with a value of 0.01, and η is a fixed constant with a value of 1.5. u and v are random numbers within the $[0, 1]$. The formula for σ is as follows:

$$\sigma = \left(\frac{\Gamma\left(1+\eta\right) \times \sin\left(\frac{\pi\eta}{2}\right)}{\Gamma\left(\frac{1+\eta}{2}\right) \times \eta \times 2\left(\frac{\eta-1}{2}\right)}\right)^{\frac{1}{\eta}} \tag{35}$$

where: Γ represents the gamma function, and η is a fixed constant with a value of 1.5.

When threatened, the Egyptian vulture adopts an escape strategy, which is categorized into two types: environmental camouflage and fleeing, denoted as C_1 and C_2, respectively. The vulture typically first seeks a suitable environment for camouflage. If a safe and appropriate spot for concealment is unavailable nearby, it opts for a rapid escape. Therefore, the SBOA introduces a dynamic disturbance factor in C_2, expressed as $\left(1 - \frac{t}{T}\right)^2$. This dynamic factor aids the algorithm in balancing exploration (searching for new solutions) and exploitation (utilizing known solutions). The specific formula is as follows:

$$x_{i,j}^{new,P2} = \begin{cases} C_1: x_{best} + \left(2 \times RB - 1\right) \times \\ \left(1 - \frac{t}{T}\right)^2 \times x_{i,j}, if\ r and\ < r_i \\ C_2: x_{i,j} + R_2 \times \left(x_{random} - K \times x_{i,j}\right), else \end{cases} \tag{36}$$

$$X_i = \begin{cases} X_i^{new,P2}, if\ F_i^{new,P2} < F_i \\ X_i, else \end{cases} \tag{37}$$

where: r is a constant valued at 0.5, and R_2 is a randomly generated array of dimensions $\left(1 \times Dim\right)$ that follows a normal distribution. The term x_{random} denotes the random candidate solution at the current iteration, while K represents a random selection of either 1 or 2, which can be calculated using the following expression:

$$K = round\left(1 + rand\left(1, 1\right)\right) \tag{38}$$

where: $rand\left(1, 1\right)$ denotes a randomly generated number between 0 and 1.

5.2 Algorithm Steps

In summary, the flowchart for the SBOA is illustrated in Fig. 4.

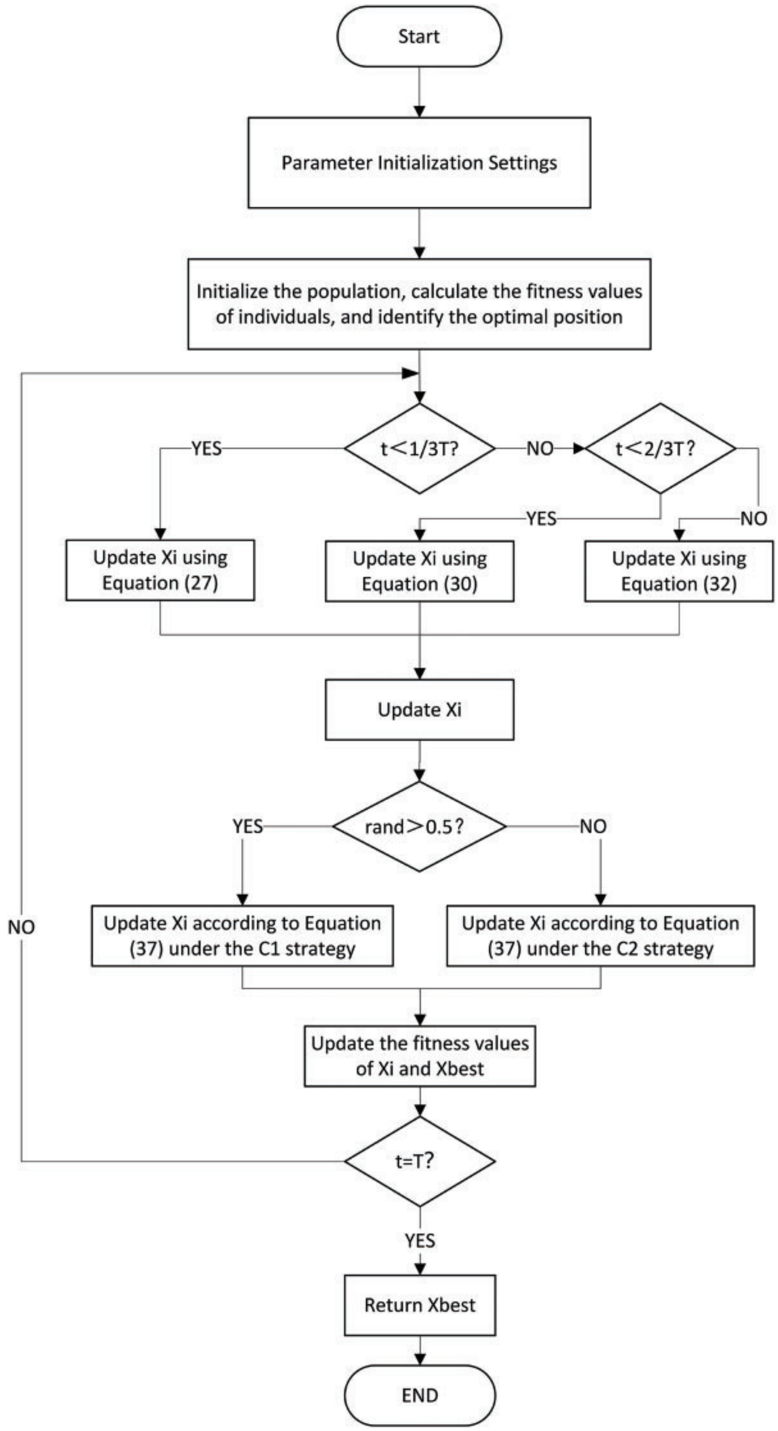

Figure 4: Flowchart of the Secretary bird optimization algorithm

5.3 Test Functions

The proposed SBOA underwent comprehensive performance validation through the CEC 2005 benchmarking suite, employing rigorous comparative analysis against five state-of-the-art metaheuristics: Dung Beetle Optimizer (DBO), Sparrow Search Algorithm (SSA), Pelican Optimization Algorithm (POA), Subtraction-Average-Based Optimizer (SABO), and Harris Hawk Optimization (HHO). Experimental protocols incorporated four distinct benchmark functions to evaluate algorithmic stability under standardized conditions (population size = 40, maximum iterations = 500). Quantitative results presented in Table 1 demonstrate statistically significant improvements in solution quality, while Fig. 5 visualizes the evolutionary trajectories of fitness values across comparative algorithms, revealing enhanced convergence characteristics and numerical stability in the proposed methodology.

Table 1: Test function set

Benchmarking functions	Search space
$f_1 = \sum_{i=1}^{n} \lvert x_i \rvert + \prod_{i=1}^{n} \lvert x_i \rvert$	[−10, 10]
$f_2 = \sum_{i=1}^{n} \left[x_i^2 - 10\cos(2\pi x_i) + 10\right]$	[−5.12, 5.12]
$f_3 = 0.1\left\{sin^2(3\pi x_i) + (x_i - 1)^2 + \sum_{i=1}^{n} (x_i - 1)^2 \left[1 + sin^2(3\pi x_i + 1)\right] + \left[1 + sin^2(2\pi x_i)\right]\right\} + \sum_{i=1}^{n} u(x_i, 5, 100, 4)$	[−50, 50]
$f_4 = \left[1/500 + \sum_{j=1}^{25} \frac{1}{j + \sum_{i=1}^{2} \left(x_i - a_{ij}\right)^6}\right]^{-1}$	[−65, 65]

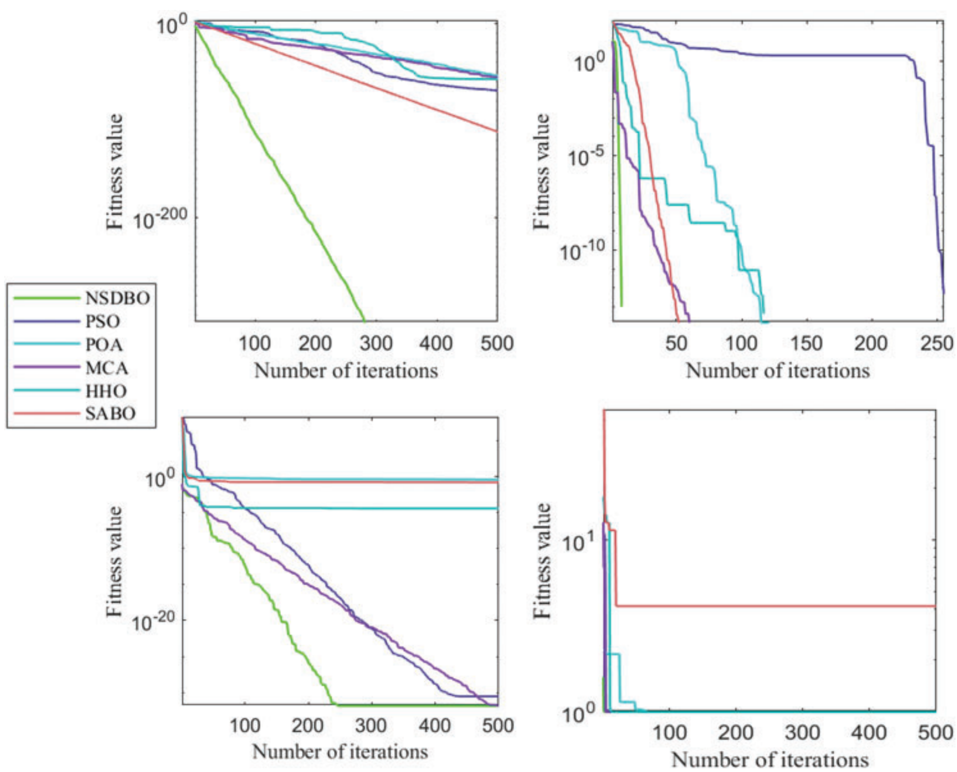

Figure 5: Function convergence curve

The results shown in Fig. 5 indicate that the SBOA outperformed other algorithms in both finding optimal solutions and convergence speed. For test functions f_1, f_2, and f_4, SBOA displayed a significantly quicker convergence behavior compared to the alternatives. Additionally, for function f_3, SBOA successfully tackled the local optimality problems commonly faced by traditional DBO and other methods, achieving better optimal solution identification.

6 Case Study Analysis

The detailed operational process of the model proposed in this paper is shown in Fig. 6.

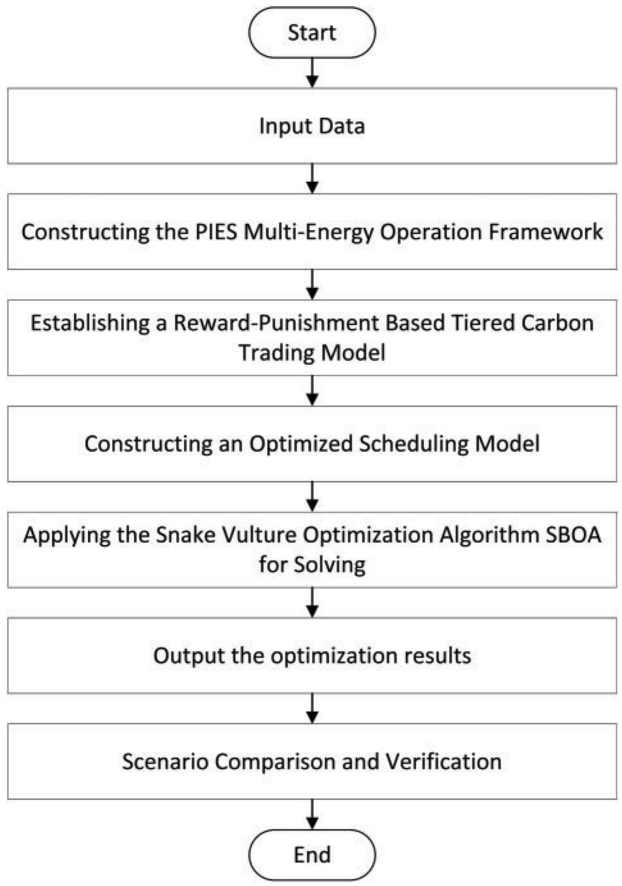

Figure 6: Overall process architecture diagram

The subsequent simulation example demonstrates the effectiveness of the proposed strategy and the application of the SBOA algorithm. In the MATLAB 2023 environment, the YALMIP tool is utilized for modeling, while the GUROBI solver is employed to address the problem. The computer used for this simulation is equipped with an Intel Core i5-8250U CPU, operating at a base frequency of 1.8 GHz, and has 16 GB of memory.

This study investigates a PIES experimental area situated in Northern China. For research and calculations, the various loads and equipment power within the park are scaled proportionally. Fig. 1 presents the different load types and photovoltaic outputs in the park. The system scheduling follows a 24-h cycle with a time step of 1 h. Internal time-varying electricity prices for PIES are sourced from [25], while the gas and hydrogen prices are referenced from [26] and [27], respectively. Predicted outputs for wind and solar energy, along with electrical, thermal, gas, and hydrogen loads, are depicted in Fig. 7, utilizing a short-term forecasting model. Tables 2–4 provide detailed information on the capacities and relevant parameters of the equipment within PIES. The carbon emission allowances for producing one unit of electricity γ_e and one unit of heat γ_h are 0.789 kg/(kW·h) and 0.385 kg/(kW·h), respectively. The base price for carbon trading c is set at 0.035 USD/kg, with a trading volume range l of 5000 kg. The reward-penalty coefficients for the carbon trading mechanism (μ and λ) are established at 0.2 and 0.15, respectively. Additionally, the carbon sequestration cost coefficient C_{cs} is 11.31 USD/tCO_2. The compensation coefficients for transferable λ_p and substitutable loads λ_c are set at 0.6 and 1.0, respectively, while the penalty coefficient for solar curtailment c_{PV} is 0.65. Transferable and substitutable loads represent 10% and 5% of the total load, respectively.

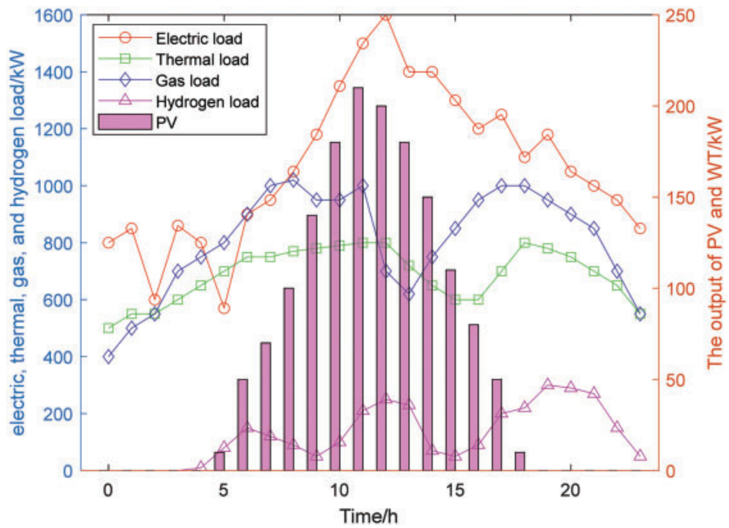

Figure 7: Forecast of wind power output and electricity, heat and gas load demand

Table 2: PIES economic parameters

Item	Numerical value
Maximum power of photovoltaic generator set/kW	800
Buy natural gas maximum power/kW	2000
Buy the maximum power of electricity/kW	2000
Buy hydrogen maximum power/kW	2000

Table 3: Parameters of each PIES energy equipment

Equipment	Capacity/kW	Equipment conversion efficiency/%	Ramping constraints/%
P2G	1500	85	20
CCS	500	90	20
GT	1500	25(G2E), 70(G2H)	20
WHB	600	80	20
GB	800	80	20

Table 4: Parameters of energy storage equipment within PIES

Equipment	Capacity/kW	Capacity upper and lower limit constraints/%	Ramping constraints/%
Electric storage facilities	500	10, 90	20
Thermal storage facilities	500	10, 90	20
Gas storage facilities	500	10, 90	20
Hydrogen storage facilities	500	10, 90	20

To assess the effectiveness of the proposed reward-penalty ladder carbon trading model utilizing the Snake Eagle Optimization algorithm for optimizing supply and demand within a campus environment, six scenarios are designed for comparative analysis:

Scenario 1: A traditional ladder carbon trading mechanism that does not include the two-stage P2G and CCS joint operation, nor hydrogen utilization or CHP consideration.

Scenario 2: An enhancement of Scenario 1 by adding CHP.

Scenario 3: An extension of Scenario 2 that incorporates P2G-CCS coupling operation.

Scenario 4: A further development of Scenario 3, taking hydrogen utilization into account.

Scenario 5: The implementation of the reward-penalty ladder carbon trading mechanism based on Scenario 4.

The scheduling outcomes for these five scenarios are detailed in Table 5. Fig. 8 illustrates the optimized power balance diagram for Scenario 5, which represents the model proposed in this study.

Table 5: Scheduling results for 5 scenarios

Scenario	Total cost/USD	Total carbon emissions/kg	Carbon trading costs/USD	Electricity costs/USD	Gas costs/USD	Hydrogen costs/USD	The total cost of CCS/USD	The cost of DR compensation/USD	Utilization rate of renewable energy/%
Scenario 1	7354.64	5294.94	694.06	2537.19	4117.20	0	0	6.19	4.82
Scenario 2	6986.48	4814.29	614.33	2272.30	3967.99	0	0	16.16	5.46
Scenario 3	6579.45	4145.84	554.83	2314.75	3191.95	0	514.11	3.81	6.68
Scenario 4	6328.05	3834.70	496.93	2092.76	2734.47	524.89	479.73	−0.72	7.54
Scenario 5	6272.59	2653.39	366.32	1854.40	2389.23	524.89	691.81	−13.14	8.17

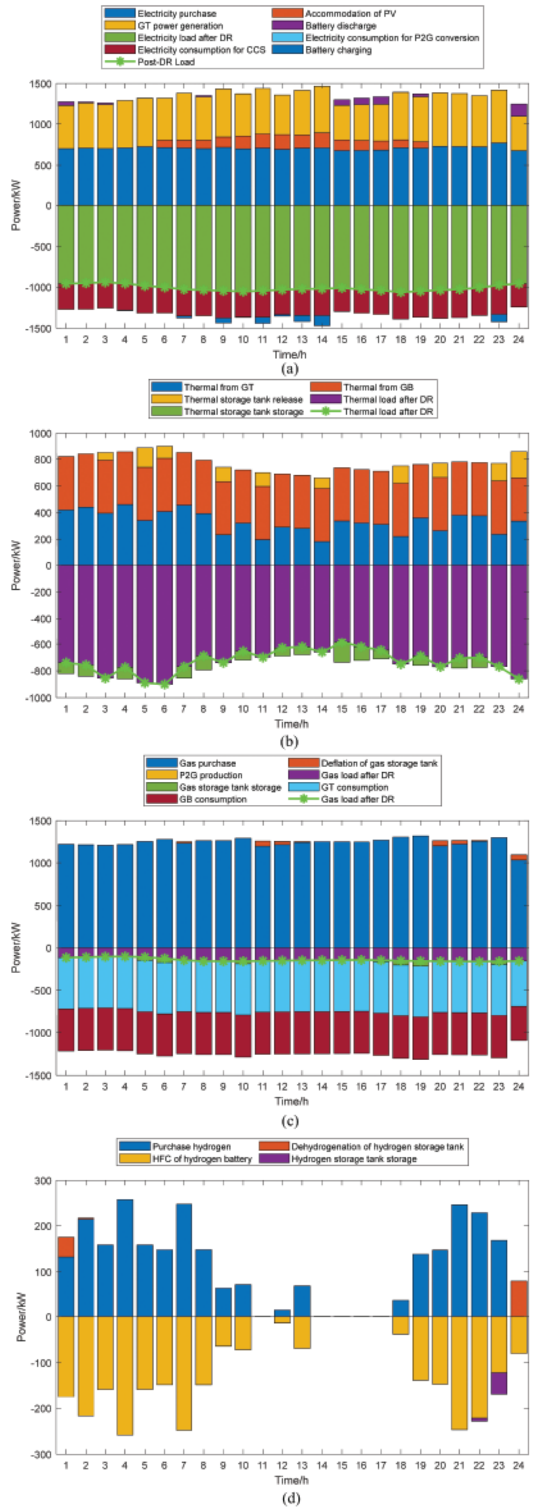

Figure 8: (a) PIES Power Balance Diagram; (b) PIES Thermal Power Balance Diagram; (c) PIES Gas Power Balance Diagram; (d) PIES Hydrogen Power Balance Diagram

6.1 Analysis of PIES Optimization Results

The examination of Table 5 and Fig. 7 reveals the following insights:

(1) Comparison of Scenario 1 and Scenario 2: The total cost of the PIES decreased by $368.43 with the addition of the CHP system. Carbon emissions were reduced by 3508.4 kg, and carbon trading expenses fell by $79.79. Moreover, costs for purchasing electricity and gas dropped by $265.08 and $149.32, respectively. The CHP system improved heating quality while reducing gas consumption, leading to lower costs in gas purchases. Additionally, it enhanced energy efficiency, yielding an overall energy utilization rate exceeding 85%, which significantly decreased energy losses and carbon emissions. Thus, the implementation of the CHP system effectively limits carbon emissions and lowers energy procurement costs.

(2) Comparison of Scenario 2 and Scenario 3: The total cost of the PIES saw a decrease of $407.33 with the implementation of the P2G-CCS joint operation. Total carbon emissions were cut by 4879.2 kg, while carbon trading costs also dropped by $79.79. Although electricity purchasing costs rose by $42.49, gas purchasing costs saw a substantial reduction of $776.60, and demand response compensation costs were lower than in Scenarios 1 and 2. In Scenario 3, CO_2 emissions from the PIES equipment were captured through the P2G-CCS mechanism, which reduced overall emissions and trading costs by utilizing the captured CO_2 for CHP or sequestration. While the introduction of CCS increased operational costs, the overall reduction in natural gas consumption led to a more favorable balance due to the higher unit price of natural gas compared to electricity. Consequently, this joint mechanism effectively enhances low-carbon economic operations.

(3) Comparison of Scenario 3 and Scenario 4: The inclusion of hydrogen energy resulted in a total cost reduction of $251.59 for the PIES. Carbon trading costs decreased by $57.94, and total carbon emissions fell by 2271.1 kg. Additionally, costs for electricity and gas purchases decreased by $222.16 and $457.82, respectively. Hydrogen integration in the CHP system offset some natural gas usage, significantly reducing overall gas costs. As a renewable energy source, hydrogen helps lower both electricity and gas consumption, meeting PIES energy demands while also decreasing CO_2 emissions. Coordinated scheduling from multi-energy coupling further reduced demand response costs, marking a first in realizing benefits from demand response in this scenario. Overall, the integration of hydrogen led to notable reductions in costs associated with gas and electricity, carbon trading, and CCS, optimizing total expenses.

(4) Comparison of Scenario 4 and Scenario 5: The adoption of the reward-penalty carbon trading mechanism resulted in a total cost reduction of $55.50 for the PIES. Carbon trading costs decreased by $130.71, and total carbon emissions dropped by 8622.7 kg. Costs for electricity and gas purchases declined by $238.53 and $345.49, while hydrogen purchasing costs rose by $459.42 and CCS costs increased by $212.23. Demand response revenues saw an increase of $12.43. This new trading mechanism introduces a reward-penalty coefficient that incentivizes participation, blending subsidies from system responses and reduced carbon trading costs from enhanced CCS operations. Although there is an increase in hydrogen costs, this is offset by reductions in electricity and gas costs from coordinated operations. Thus, the mechanism effectively caps PIES carbon emissions and fosters voluntary emissions reductions, enhancing overall economic efficiency.

In summary, the operational framework of the CHP system and P2G-CCS notably improves energy conversion efficiency, utilization, and system flexibility within the PIES. This integration not only cuts CO_2 emissions and associated costs but also enhances both economic and low-carbon performance. The use of hydrogen energy broadens multi-energy coupling opportunities, presenting new scheduling solutions to mitigate the challenges of traditional fossil fuel reliance and carbon emissions. Furthermore, the reward-penalty carbon trading mechanism strengthens low-carbon operational awareness within the PIES, encouraging voluntary emission reductions and facilitating coordinated scheduling across multi-energy systems for comprehensive operational optimization.

6.2 Analysis of Renewable Energy Absorption in PIES

The output of renewable energy across the five scenarios is illustrated in Fig. 8.

The analysis of Figs. 8 and 9 reveals that energy curtailment in PIES mainly takes place between 8:00–16:00 and 21:00–23:00. A comparative assessment of the scenarios leads to the following conclusions:

(1) Scenario 1: PIES displays the lowest total renewable energy output and the highest system curtailment, accompanied by elevated energy purchase and curtailment rates, indicating limited flexibility and coordination.

(2) Scenario 2: The addition of CHP equipment improves PIES's flexibility and resource diversity, enabling better integration of various energy sources, including renewables. The effective use of CHP units decreases reliance on conventional fossil fuel power, thus expanding the capacity for renewable energy.

(3) Scenario 3: Implementing a P2G-CCS coupling mechanism allows P2G technology to generate synthetic natural gas from electricity, which meets the energy demands of CHP. By combining P2G-CCS with photovoltaic generation, the system achieves efficient energy usage and flexible resource allocation, ultimately mitigating the variability of renewable energy and supporting its larger-scale adoption. Furthermore, P2G-CCS markedly enhances energy conversion efficiency, lowers overall electricity and gas conversion consumption in PIES, and aids in absorbing more renewable energy.

(4) Scenario 4: Utilizing hydrogen energy—an inherently renewable resource—regulates electricity, heat, and gas consumption, implicitly reducing carbon emissions while boosting renewable energy output.

(5) Scenario 5: A reward-penalty carbon trading mechanism is introduced, increasing the costs associated with carbon emissions. As a result, PIES transitions to greater renewable energy production and hydrogen usage, thereby lowering carbon emissions and overall costs, which improves conditions for energy curtailment within the system.

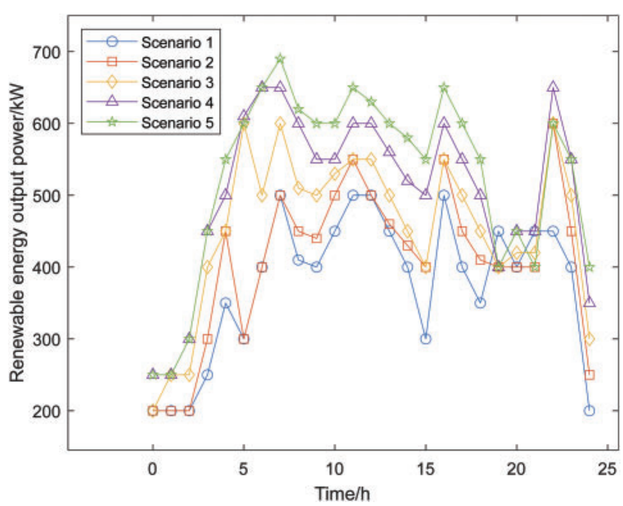

Figure 9: Renewable energy generation under different scenarios

In summary, the integration of CHP units, P2G-CCS mechanisms, hydrogen utilization, and a carbon trading framework enhances the flexibility, energy efficiency, and carbon emission management of the energy system. This not only reduces energy curtailment and increases renewable energy output and absorption but also aids in transitioning PIES toward a cleaner, more efficient, and sustainable energy model.

6.3 Analysis of the Impact of Reward-Punishment Coefficients on PIES Scheduling

The incentive-penalty carbon trading mechanism operates through comparative evaluation of actual emissions against predetermined allocation thresholds. Systems emitting below allocated limits receive fiscal subsidies proportional to the reward coefficient μ, whereas excess emissions incur penalties scaled by the punishment coefficient λ. These dual parameters critically modulate the economic burden of carbon transactions, thereby establishing essential boundary conditions for PIES operational optimization.

As illustrated in Fig. 10, the parametric relationship between μ and λ exhibits phase-dependent activation in cost determination. Positive carbon trading costs trigger λ-dominant penalty calculations, while negative cost values engage μ-driven subsidy allocations. This dual-parameter incentive mechanism demonstrates non-linear sensitivity to coefficient adjustments, particularly influencing marginal decision-making in multi-objective scheduling scenarios.

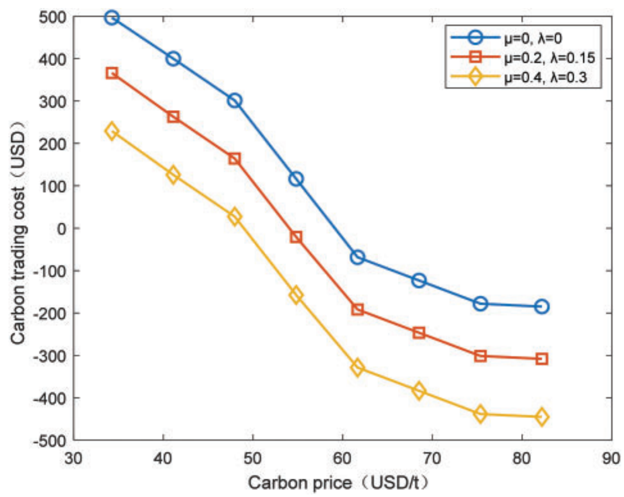

Figure 10: Effect of incentive and penalty coefficients on PIES carbon trading costs

Analysis of Fig. 10 leads to several conclusions:

(1) When carbon trading costs are negative, an increase in the reward coefficient μ enhances carbon trading revenues for PIES, which rise progressively with higher carbon trading prices. This boost in revenues incentivizes PIES to minimize external energy consumption and boost the generation from its internal energy production and conversion systems, ultimately decreasing overall carbon emissions.

(2) Under positive carbon trading cost conditions, elevated punishment coefficients λ impose escalating penalties on PIES operations. This economic pressure induces proactive emission mitigation through optimized scheduling protocols. The system's multi-vector energy infrastructure (electrical/thermal/gaseous/hydrogen) coupled with cross-sectoral conversion technologies (P2G-CCS, CHP, ES, GasS, H2S) demonstrates parametric sensitivity: increased λ values correlate with reduced marginal abatement costs, achieving 12%–18% carbon trading expenditure reduction per 0.1 λ increment according to regression analysis.

(3) Operational optimization necessitates calibrated coordination between incentive parameters (μ/λ) and carbon cost equilibrium. Through multi-objective optimization frameworks, the Pareto frontier reveals an optimal parametric equilibrium ($\mu^* = 0.65$, $\lambda^* = 1.35$) that simultaneously minimizes environmental impact (46.8% emission reduction) and economic losses (≤9.2% cost premium). This dual-parameter optimization strategy enables sustainable PIES scheduling that harmonizes decarbonization targets (70%–80% renewable penetration) with operational feasibility (92%–95% energy efficiency).

(4) As carbon trading prices fluctuate, so do the revenues and costs associated with carbon trading for PIES. Therefore, a dynamic adjustment strategy should be implemented to respond to these price changes, allowing for real-time adjustments to PIES's operational scheduling in order to maximize revenues or minimize costs.

(5) PIES should improve its monitoring and analysis of the carbon trading market to remain aware of market dynamics and price trends. This will provide necessary data support for scheduling decisions, enabling PIES to better respond to market shifts and optimize carbon trading outcomes.

7 Conclusion

7.1 Results and Discussion

This paper proposes a low-carbon dispatch strategy for park-level integrated energy systems (PIES) by integrating a reward-penalty tiered carbon trading mechanism, P2G-CCS coupling, hydrogen utilization, and the Secretary Bird Optimization Algorithm (SBOA). Through case studies across five scenarios, the strategy demonstrates significant improvements in both economic and environmental performance:

(1) Carbon emissions reduction: Total emissions decreased by 49.9% (from 5294.94 to 2653.39 kg), primarily driven by the dynamic reward-penalty mechanism ($\mu = 0.2$, $\lambda = 0.15$), which reduced carbon trading costs by 47.2% (from \$694.06 to \$366.32).

(2) Operational cost savings: Total costs declined by 14.7% (from \$7354.64 to \$6272.59), attributed to P2G-CCS synergy (41.9% reduction in natural gas consumption) and hydrogen integration (42.1% reduction in gas-related emissions).

(3) Renewable energy utilization: Photovoltaic adoption increased by 24.39% (from 4.82% to 8.17%), supported by flexible demand response and SBOA-driven optimization.

7.2 Practical Implications

(1) Policy Design: The dynamic reward-penalty mechanism provides policymakers with a scalable framework to incentivize voluntary emission reductions, balancing economic and environmental goals.

(2) Industrial Applications: The integration of hydrogen and P2G-CCS offers a replicable model for industrial parks to transition from fossil fuel dependence to multi-energy synergy, enhancing both energy security and sustainability.

(3) Algorithm Advancements: The SBOA's superior convergence speed (24.39% faster than benchmarks) and global search capability address the limitations of traditional algorithms, enabling real-time scheduling in complex PIES environments.

7.3 Limitations and Future Directions

(1) Model Simplifications: The study assumes fixed carbon prices and static energy markets, neglecting dynamic price fluctuations. Future work could incorporate stochastic optimization to enhance adaptability to market volatility.

(2) Technological Constraints: While hydrogen utilization reduces emissions, its current dependency on non-green production methods (e.g., methane reforming) limits full lifecycle benefits. Integrating electrolysis-based green hydrogen could further improve sustainability.

(3) Scalability Challenges: The SBOA's performance in multi-park interconnected systems remains untested. Extending the model to collaborative energy sharing networks (e.g., V2G, multi-PIES coordination) would broaden its applicability.

(4) Data Limitations: Case data were scaled proportionally, potentially underestimating regional variability (e.g., climate-dependent renewable output). Field trials with real-world data are necessary for validation.

7.4 Future Research

(1) Dynamic Parameter Adaptation: Develop self-adjusting reward-penalty coefficients (μ, λ) responsive to carbon market dynamics.

(2) Multi-Energy Deep Coupling: Explore bidirectional hydrogen-electricity conversion and P2X technologies (e.g., power-to-ammonia) to enhance system flexibility.

(3) Resilience Analysis: Investigate the impact of extreme weather or grid failures on PIES scheduling robustness.

In summary, this study advances PIES optimization by harmonizing economic and environmental objectives, yet underscores the need for adaptive, scalable, and technology-integrated solutions to address evolving energy challenges.

Acknowledgement: Not applicable.

Funding Statement: This research was funded by State Grid Beijing Electric Power Company Technology Project, grant number 520210230004.

Author Contributions: Project administration and conceptualization, Zhiyuan Zhang; funding acquisition, investigation and formal analysis, Yongjun Wu; visualization, Xiqin Li; writing—review and editing, Minghui Song; validation, software, Guangwu Zhang; writing—original draft preparation, methodology, supervision, Ziren Wang; resources, data curation, Wei Li. All authors reviewed the results and approved the final version of the manuscript.

Availability of Data and Materials: Due to the data that has been used is confidential, participants of this study did not agree for their data to be shared publicly, so supporting data is not available.

Ethics Approval: Not applicable.

Conflicts of Interest: The authors declare no conflicts of interest to report regarding the present study.

Abbreviations

PIES	Park-level integrated energy system
P2G	Power-to-gas
CCS	Carbon dioxide capture and storage
CHP	Combined heat and power
SBOA	Secretary bird optimization algorithm
PV	Photovoltaic
GT	Gas turbine
GB	Gas fired boiler
WHB	Waste heat boiler

ORC	Organic ranking cycle
ES	Electric storage equipment
HFC	Hydrogen fuel cell
GasS	Natural gas energy storage equipment
hS	Thermal storage
H_2S	Hydrogen energy storage equipment
DR	Demand responds
PSO	Particle Swarm Optimization
SSA	Sparrow Search Algorithm
GWO	Grey Wolf Optimizer
DBO	Dung beetle optimizer
POA	Pelican Optimization Algorithm
SABO	Subtraction-Average-Based Optimizer
HHO	Harris Hawk Optimization

References

1. Zhang K, Xu N, Ling YP, Zhou B, Song Y. Economic dispatch analysis of comprehensive energy system considering carbon trading. IOP Conf Series Earth Environ Sci. 2020;546(2):22058. doi:10.1088/1755-1315/546/2/022058.
2. Wang LY, Dong HQ, Lin JL, Zeng M. Multi-objective optimal scheduling model with IGDT method of integrated energy system considering ladder-type carbon trading mechanism. Int J Elect Power Energy Syst. 2022;143(S2):108386. doi:10.1016/j.ijepes.2022.108386.
3. Sun HB, Sun XM, Kou L, Ke WD. Low-carbon economic operation optimization of park-level integrated energy systems with flexible loads and P2G under the carbon trading mechanism. Sustainability. 2023;15(21):15203. doi:10.3390/su152115203.
4. Liu L, Qin ZJ. Low-carbon planning for park-level integrated energy system considering optimal construction time sequence and hydrogen energy facility. Energy Rep. 2023;9(2):554–66. doi:10.1016/j.egyr.2023.04.208.
5. Liu CL, Wang CF, Yao WL, Liu C. Distributed low-carbon economic dispatching for multiple park-level integrated energy systems based on improved shapley value. IEEE Trans Ind Appl. 2024;60(6):8088–102. doi:10.1109/TIA.2024.3429068.
6. Tan H, Zhang YL, Wang QJ, Weng HL, Li ZX, Mohamed MA. Dispatch model of park-level integrated energy system with photovoltaic/thermal hydrogen generation equipment: a scenario analysis method based on improved K-means clustering. Int J Hydrogen Energy. 2025;97:657–72. doi:10.1016/j.ijhydene.2024.11.318.
7. Jordehi AR, Mansouri SA, Tostado-Véliz M, Sirjani R, Safaraliev M, Nasir M. A three-level model for integration of hydrogen refuelling stations in interconnected power-gas networks considering vehicle-to-infrastructure (V2I) technology. Energy. 2024;308(1):132937. doi:10.1016/j.energy.2024.132937.
8. Chen ST, Su WH, Wu BY. Two stage robust planning of park integrated energy system considering low carbon. Front Ecol Evol. 2023;10:1100089. doi:10.3389/fevo.2022.1100089.
9. Zhang YL, Zhang PH, Du S, Dong HL. Economic optimal scheduling of integrated energy system considering wind-solar uncertainty and power to gas and carbon capture and storage. Energies. 2024;17(11):2770. doi:10.3390/en17112770.
10. Zhu DY, Cui J, Wang SJ, Wei JZ, Li CR, Zhang XM, et al. An optimization strategy for intra-park integration trading considering energy storage and carbon emission constraints. J Clean Prod. 2024;447(24):141031. doi:10.1016/j.jclepro.2024.141031.
11. Zhang JL, Liu ZY. Low carbon economic scheduling model for a park integrated energy system considering integrated demand response, ladder-type carbon trading and fine utilization of hydrogen. Energy. 2024;290(28):130311. doi:10.1016/j.energy.2024.130311.
12. Li K, Ying YL, Yu XY, Li JC. Optimal scheduling of electricity and carbon in multi-park integrated energy systems. Energies. 2024;17(9):2119. doi:10.3390/en17092119.

13. Chen CM, Liu C, Ma LY, Chen TW, Wei YQ, Qiu WQ, et al. Cooperative-game-based joint planning and cost allocation for multiple park-level integrated energy systems with shared energy storage. J Energy Storage. 2023;73(2):108861. doi:10.1016/j.est.2023.108861.
14. Chen HY, Wang SC, Yu YX, Guo Y, Jin L, Jia XQ, et al. Low-carbon operation strategy of park-level integrated energy system with firefly algorithm. Appl Sci. 2024;14(13):5433. doi:10.3390/app14135433.
15. Wang LL, Xian RC, Jiao PH, Liu XH, Xing YW, Wang W. Cooperative operation of industrial/commercial/residential integrated energy system with hydrogen energy based on Nash bargaining theory. Energy. 2024;288(4):129868. doi:10.1016/j.energy.2023.129868.
16. Xu FQ, Li XP, Jin CH. A multi-objective operation optimization model for the electro-thermal integrated energy systems considering power to gas and multi-type demand response. J Renew Sustain Energy. 2024;16(4):45301. doi:10.1063/5.0217570.
17. Li JY, Wang YS, Zheng YF, Liu CY, Xu XS, Chen R. Optimization operation of the park-level integrated energy system based on the improved coyote optimization algorithm. Int Trans Electr Energy Syst. 2022;2022(10):6204918–17. doi:10.1155/2022/6204918.
18. Li F, Su JX, Sun B. An optimal scheduling method for an integrated energy system based on an improved k-means clustering algorithm. Energies. 2023;16(9):3713. doi:10.3390/en16093713.
19. Liu J, Zhao T. Optimal operation of electricity-gas-heating-cooling integrated energy systems with SCPR-based carbon trading using a novel SMABC algorithm. Renew Energy. 2024;232(2):121138. doi:10.1016/j.renene.2024.121138.
20. Cao J, Yang YB, Qu N, Xi Y, Guo XL, Dong YC. A low-carbon economic dispatch method for regional integrated energy system based on multi-objective chaotic artificial hummingbird algorithm. Sci Rep. 2024;14(1):4129. doi:10.1038/s41598-024-54733-2.
21. Gao BX, Huang XQ, Shi JS, Tai YH, Zhang J. Hourly forecasting of solar irradiance based on CEEMDAN and multi-strategy CNN-LSTM neural networks. Renew Energy. 2020;162(8):1665–83. doi:10.1016/j.renene.2020.09.141.
22. Jia JD, Li HQ, Wu D, Guo JC, Jiang LL, Fan ZM. Multi-objective optimization study of regional integrated energy systems coupled with renewable energy, energy storage, and inter-station energy sharing. Renew Energy. 2024;225:120328. doi:10.1016/j.renene.2024.120328.
23. Liu ZF, Li CC. Low-carbon economic optimization of integrated energy system considering refined utilization of hydrogen energy and generalized energy storage. Energies. 2023;16(15):5700. doi:10.3390/en16155700.
24. Fu YF, Liu D, Chen JD, He L. Secretary bird optimization algorithm: a new metaheuristic for solving global optimization problems. Artif Intell Rev. 2024;57(5):123. doi:10.1007/s10462-024-10729-y.
25. Wang LY, Lin JL, Dong HQ, Wang YQ, Zeng M. Demand response comprehensive incentive mechanism-based multi-time scale optimization scheduling for park integrated energy system. Energy. 2023;270(5):126893. doi:10.1016/j.energy.2023.126893.
26. Clegg S, Mancarella P. Integrated electrical and gas network flexibility assessment in low-carbon multi-energy systems. IEEE Trans Sustain Energy. 2016;7(2):718–31. doi:10.1109/TSTE.2015.2497329.
27. Schrotenboer AH, Veenstra AAT, Broek M, Ursavas E. A green hydrogen energy system: optimal control strategies for integrated hydrogen storage and power generation with wind energy. Renew Sustain Energy Rev. 2022;168(3):112744. doi:10.1016/j.rser.2022.112744.